Synthesis and Electrocatalytic Activity of Bismuth Tungstate Bi2WO6 for Rhodamine B Electro-Oxidation

Hassan Ait Ahsaine, Amal Baqais, Madjid Arab, Bahcine Bakiz, Abdeljalil Benlhachemi

catalysts

MDPI

Article

Synthesis and Electrocatalytic Activity of Bismuth Tungstate Bi_2WO_6 for Rhodamine B Electro-Oxidation

Hassan Ait Ahsaine [1,*], Amal BaQais [2], Madjid Arab [3], Bahcine Bakiz [4] and Abdeljalil Benlhachemi [4]

[1] Laboratoire de Chimie Appliquée des Matériaux, Faculty of Sciences, Mohammed V University in Rabat, Rabat BP 1014, Morocco
[2] Department of Chemistry, College of Science, Princess Nourah Bint Abdulrahman University, P.O. Box 84428, Riyadh 11671, Saudi Arabia
[3] Aix Marseille University, University Toulon, CNRS, IM2NP, CS 60584, CEDEX 9, F-83041 Toulon, France
[4] Laboratoire Matériaux et Environnement LME, Faculté des Sciences, Université Ibn Zohr, Cité Dakhla, Agadir BP 8106, Morocco
* Correspondence: h.aitahsaine@um5r.ac.ma

Abstract: Herein, we have synthesized different BWO samples at different temperatures and evaluated their electrochemical oxidation of Rhodamine B dye in an aqueous medium. The prepared samples were characterized using X-ray diffraction combined with Rietveld refinements, scanning electron microscope coupled with energy dispersive elemental mapping, and thermogravimetric and differential thermal analyses. All the samples crystallize in the orthorhombic $Pca2_1$ structure. The crystallite size increased with temperature. The calculated surface areas from the XRD data ranged from 38 to 7 $m^2\ g^{-1}$ for BWO-600 to BWO-900, respectively. The optimal BWO loadings on the GCE electrode were 5×10^{-8} mol cm^{-2} recording the best electrocatalytic efficiency for RhB electrodegradation in 15 min (100%) in 0.1 M of NaCl. The BWO-600 recorded the best activity compared to other BWO samples. The electrocatalytic activity was explained by the high surface area and small crystallite size compared to the other samples. The BWO-600 showed extended electrode reutilization for up to four cycles of reuse under the reported conditions.

Keywords: electrochemical degradation; Rhodamine B; hydroxyl radicals; bismuth tungstate; electrode

Citation: Ait Ahsaine, H.; BaQais, A.; Arab, M.; Bakiz, B.; Benlhachemi, A. Synthesis and Electrocatalytic Activity of Bismuth Tungstate Bi_2WO_6 for Rhodamine B Electro-Oxidation. *Catalysts* **2022**, *12*, 1335. https://doi.org/10.3390/catal12111335

Academic Editor: Enric Brillas

Received: 28 September 2022
Accepted: 24 October 2022
Published: 1 November 2022

1. Introduction

Bismuth tungstate Bi_2WO_6 is a material of great interest because of its great utility in the manufacture of electronic components and the diversity of its applications: optical sensors, capacitors, thermistors, humidity detectors [1], and a visible-light photocatalyst that is widely studied for wastewater treatment and dye photodegradation [2]. Bismuth tungstate Bi_2WO_6 was first studied in 1992 by Knight [3] and it has attracted much attention due to its excellent physical and chemical properties such as piezoelectricity, ferroelectricity, catalysis, and nonlinear dielectric susceptibility [3–5]. Among the commonly encountered semiconductor oxides, titanium dioxide TiO_2 has been widely used for environmental remediation because of its oxidizing power, chemical stability, and low economic cost [6,7]. However, this material has limitations due to its high gap (3.2 eV), which limits the absorption of UV irradiation up to 387 nm, which only represents 4% of the solar spectral band [6–10]. Contrarily, Bi_2WO_6 has a 2.7 eV band gap, which allows it to shift absorption towards longer visible-light wavelengths (and thus towards solar-related applications). Structurally, the BWO is constituted of alternating bismuth chemical entities $Bi_2O_2^{2+}$ and Tungsten WO_4^{2-} chemical entities [11].

Pollutants based on colorant textile dyes contain bulky molecular species and complexes that can threaten human health and the surrounding ecosystems, as well as the major concern of their resistant biodegradability. These dyes are highly toxic and can lead to the contamination of fresh waters if not treated [11–18]. Consequently, several advanced

oxidation processes have been developed to overcome these emerging threats, such as adsorption, photodegradation, electrocatalytic degradation, and Fenton-like processes.

Electrocatalytic oxidation is characterized by its simple use, favorable oxidation performance for a wide spectrum of pollutants, safety, energy efficiency, easy maneuverability, and environmental applicability compared to other advanced oxidation processes [19–22]. In this regard, complete mineralization to CO_2 by mediated oxidation with reactive oxygen species (hydroxyl radical (•OH, E = 2.80 V/SHE)) is more easily achieved with the use of an electrocatalytic process, which is far more efficient than only photocatalysis [23,24]. Because it is not feasible to make high surface area working electrodes in simple electrochemical cells to enhance the efficiency of the electrocatalyst, one strategy is to prepare electroactive materials that have a relatively high overpotential for oxygen evolution reaction. Putting an organic pollutant (P) in an electrolytic cell by applying a potential, the mechanistic of the electrocatalytic pollutant removal approach can be summarized as follows:

$$P + AO_x^{+1} \rightarrow PO + AO_x$$

$$AO_x + H_2O \rightarrow AO_x(\bullet OH) + H^+ + e^-$$

$$(1/2)P + AO_x(\bullet OH) \rightarrow (1/2)POO + H^+ + e^- + AO_x$$

A direct electron transfer to the anode (A) produces (AOx) oxide, which produces adsorbed hydroxyl radicals (AO_x(•OH)) as an intermediate species in the evolution of oxygen from aqueous solution.

In this paper, we have prepared BWO powders at different temperatures ranging from 600 to 900 °C. The structural and thermal analyses were carried out using X-ray diffraction and thermogravimetric analyses. The structure of the synthesized highly crystalline powder noted as BWO-900 has been resolved and analyzed using the Rietveld refinements. The reliability factors showed an excellent match between the observed and calculated profiles. The electrocatalytic activity for the oxidation of Rhodamine B in aqueous solution has been performed and discussed.

2. Results and Discussion

2.1. X-ray Diffraction Analyses

The XRD diffraction profiles are shown in Figure 1. By analyzing the spectra obtained using WinPLOTR software, we can see the presence of several well-defined peaks, which proves that the samples are relatively well-crystallized, corresponding to the orthorhombic BWO phase referenced in the JCPDS files (JCPDS card no. 73–1126). Starting at 600 °C, we managed to synthesize a well-crystallized Bi_2WO_6. The variation in the half-value width β of the diffraction lines between the three samples can be seen. This variation is generally explained by the effect of crystallite size. The half width β decreases with increasing calcination temperature, and since the half width is inversely proportional to the crystallite size, the latter increases with calcination temperature. This might lead to a significant decrease in catalytic activity, given the decrease in the specific surface area of the samples.

The crystallite size is calculated by the Scherrer formula. By comparing these data for the samples synthesized at different calcination temperatures, we can assess the evolution of the catalytic activity, which mainly depends on crystallite size and surface area. With a simple comparison of the diffraction between the prepared samples and the referenced bismuth tungstate in the JCPDS files, we have observed a broadening of the peaks because of the size effects. Accordingly, we have calculated the crystallite size D using the Scherrer method as follows:

$$D = k\lambda/\beta\cos(\theta) \quad (1)$$

where D, λ, β, and θ are crystallite size, radiation wavelength, angular broadening of the peak, and Bragg position, respectively. K is a constant which is equal to 0.9 assuming that

the profiles are gaussian-like. The broadening β is calculated with a gaussian approximation of peak profiles using the following formula:

$$\beta^2 = (\text{FWHM})^2 - \omega^2 \quad (2)$$

FWHM and ω are the full width at half maximum of the Bragg peak of the prepared sample and the corresponding FWHM of the standard sample, respectively. The crystallite sizes of the BWO-600, BWO-700, BWO-800, and BWO-900 are 17.1, 39.2, 48.5, and 83.7 nm, respectively.

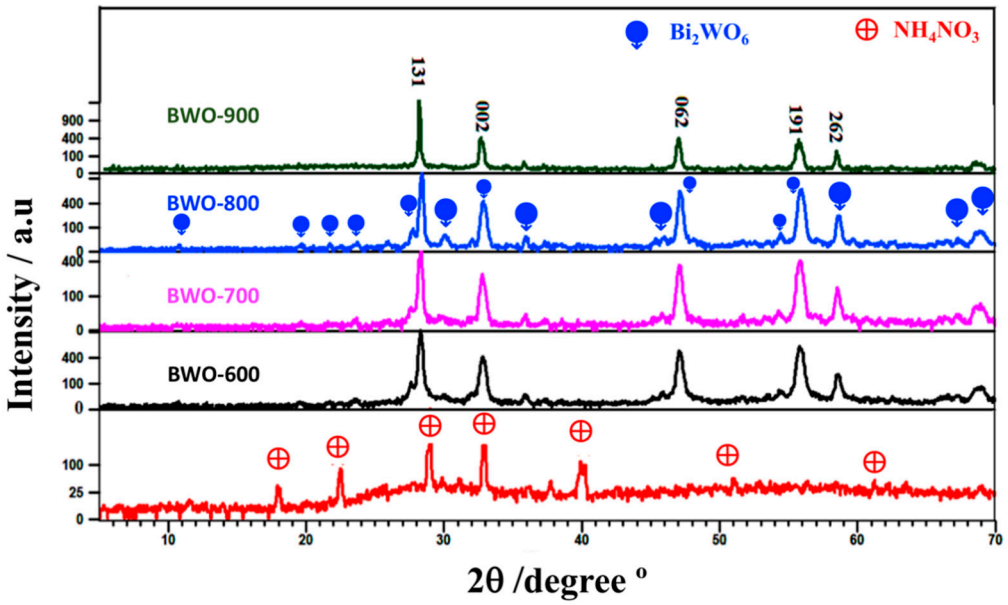

Figure 1. Diffraction profiles of the prepared materials.

The theoretical surface area S was calculated using the formula as follows:

$$S = 6/(\rho D) \quad (3)$$

where D is crystallite size using Scherrer method determined from XRD data, ρ is the density of the Bi_2WO_6. The density of the BWO calculated from Rietveld analyses is 9.2 g cm^{-3}, which corresponds to 96.8 % of the theoretical value. The calculated surface areas of the prepared electrocatalysts BWO-600, BWO-700, BWO-800, and BWO-900 are 38.13, 16.63, 13.44, and 7.79 m^2 g^{-1}, respectively. The Rietveld refinement (Figure 2) of the well crystallized sample at 900 °C for 8 h was performed by the FullProf PCR software, which allows the refinement of several parameters until the optimal factors are obtained. Table 1 summarizes the atomic positions, the obtained cell parameters, and the reliability factors. During refinement, we refined the positions of the heavy atoms Bi and W by fixing the positions of the oxygen atoms. These light atom positions cannot be refined because of the small contributions of oxygen to the structure factors. This is the reason why these coordinates were fixed during the refinements.

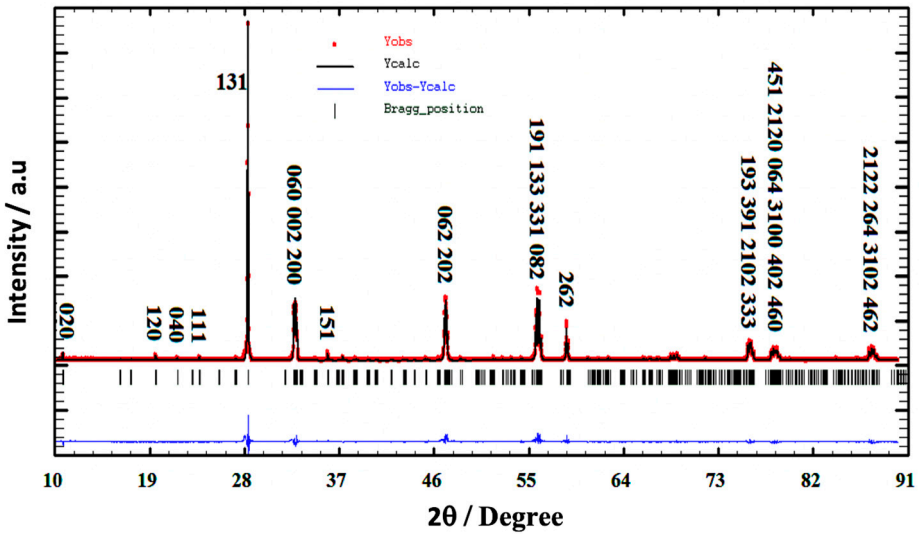

Figure 2. Rietveld refinement profiles and the corresponding Bragg positions.

Table 1. Final Rietveld parameters and atomic positions for the BWO at 900 °C.

Lattice Parameters: *a*, *b*, *c*	**Space Group**		**JCPDS Reference 79–2381**	
Volume (10^{-30} m^3)				
Sd between ()				
a = 5.431 (3)	Orthorhombic $Pca2_1$		a = 5.437	
b = 16.426 (2)			b = 16.430	
b = 5.450 (3)			c = 5.458	
V = 487.022 (3)			V = 487.634	
Reliability factors			Percentage	
$R_p = 100.\ \{\sum \mid y_i^{obs} - y_i^{calc} \mid / \sum \mid y_i^{obs} \mid\}$			6.61%	
$R_{wp} = 100.\ \{\mid \sum w_i \mid y_i^{obs} - y_i^{calc} \mid^2 / \sum w_i \mid y_i^{obs} \mid^{21/2}\}$			8.05%	
$R_{exp} = 100.\ \{[(N\text{-}P+C)/\sum w_i \mid y_i^{obs} \mid^2]^{1/2}\}$			5.69%	
$R_B = 100.\ \{\sum \mid I_k^{obs} - I_{ki}^{calc} \mid / \sum \mid I_k^{obs} \mid\}$			5.64%	
$R_F = 100.\ \{\sum \mid F_k^{obs} - F_{ki}^{calc} \mid / \sum \mid F_k^{obs} \mid\}$			5.23%	
With N, P, and C denoting the number of observations, parameters, and constraints, respectively.				
Atomic positions				
Atoms (Wyckoff)	*x*	*Y*	*z*	Biso(Å^2) (*)
Bi (1)	0.517 (3)	0.426 (2)	0.983 (3)	0.38 (3)
Bi (2)	0.473 (2)	0.078 (2)	0.969 (3)	0.60 (2)
W	0.005 (4)	0.244 (2)	0.000 (–)	0.18 (2)
O (1)	0.057 (–)	0.140 (–)	0.076 (–)	0.85 (–)
O (2)	0.259 (–)	0.999 (–)	0.263 (–)	0.69 (–)
O (3)	0.240 (–)	0.500 (–)	0.255 (–)	0.40 (–)
O (4)	0.705 (–)	0.232 (–)	0.250 (–)	0.79 (–)
O (5)	0.213 (–)	0.263 (–)	0.330 (–)	0.96 (–)
O (6)	0.561 (–)	0.359 (–)	0.561 (–)	0.69 (–)

* Biso is isotropic Debye–Waller thermal factor: $B = 8\pi 2/3(R^2)$ with R associated with vibration amplitudes of atoms.

2.2. Scanning Electron Microscope Analyses

SEM micrographs (Figure 3) showed that the shape and morphology of the BWO at 600, 700, and 800 °C are identical; it consists of regular rounded-shaped grains. The sample

treated at 900 °C had a different heterogeneous irregular shape of rounded particles and polyhedral shapes. This morphology can be explained by the role of elevated temperatures in welding together smaller particles to form larger ones. The approximate calculated average grain sizes for the prepared samples are 25, 47, 72, and 135 nm for BWO-600, BWO-700, BWO-800, and BWO-900, respectively. This is in agreement with the crystallite sizes extracted from the XRD patterns.

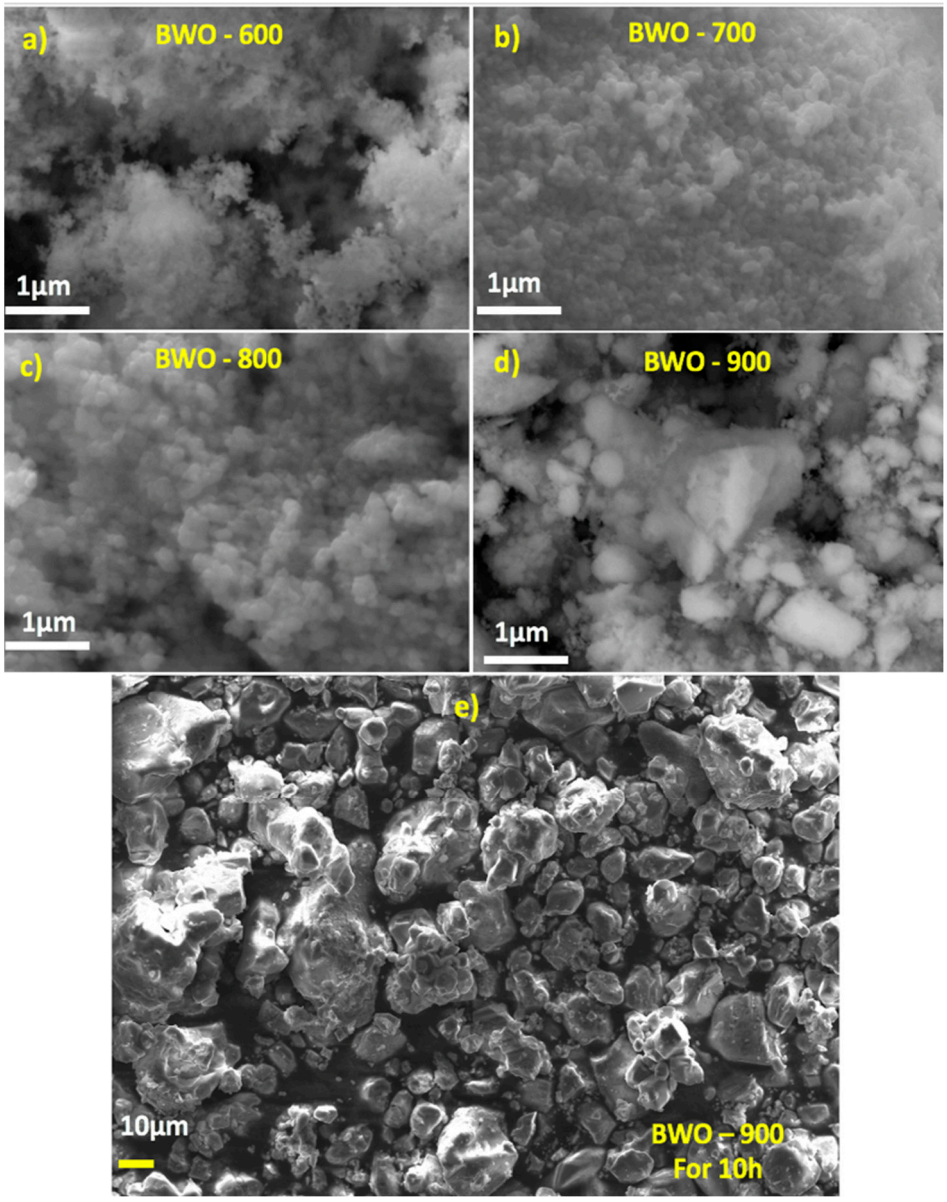

Figure 3. SEM micrographs of the prepared BWO at different temperatures.

The energy dispersive spectroscopy mapping confirmed the composition of the BWO-600, which is composed of Bi, W, and O atoms (Figure 4), with a ratio of 2:1:6. The calculated composition from EDS was in agreement with the nominal composition of the BWO sample.

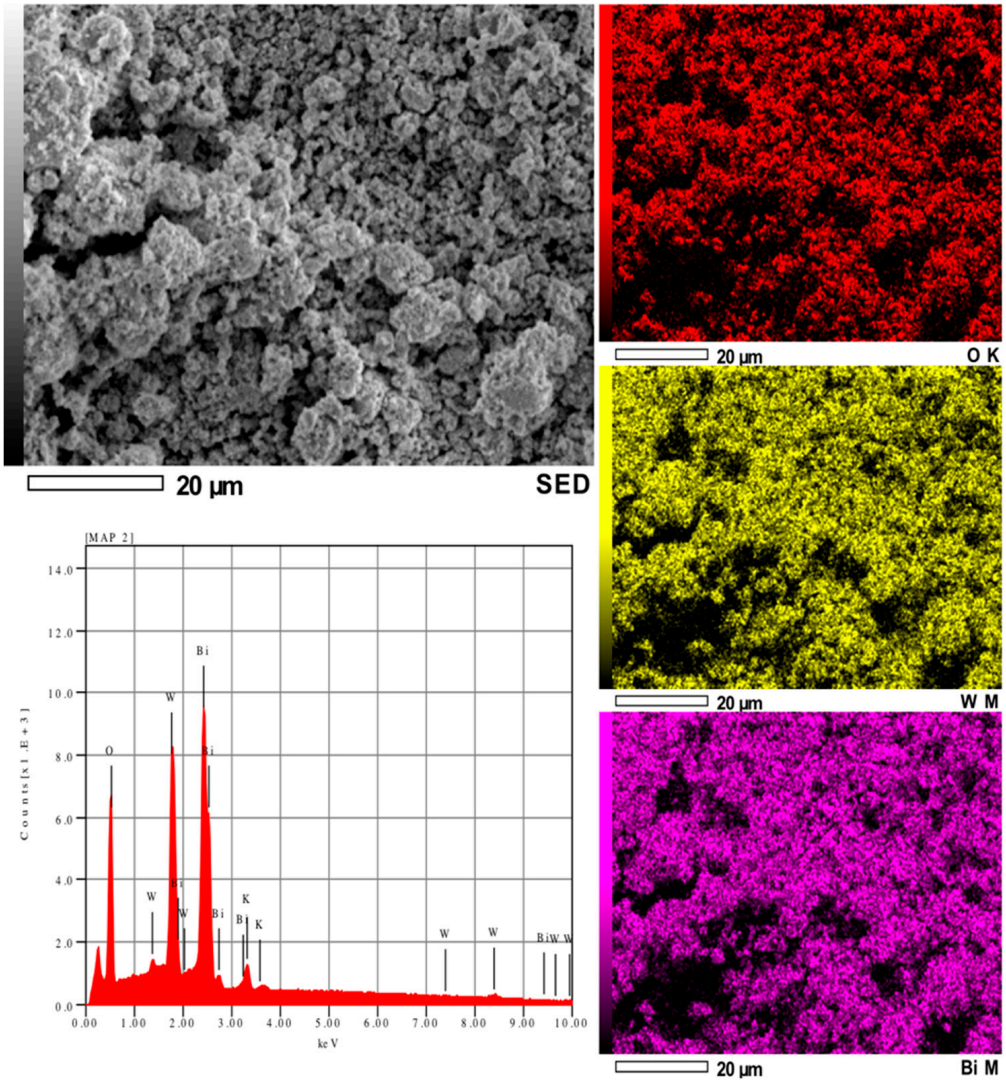

Figure 4. The corresponding EDS and the mapping of the O, W, and Bi elements (BWO-600), respectively.

2.3. Thermogravimetric Analyses

The thermal study of the white paste precipitate was carried out in order to optimize the processing conditions and to identify the mass losses related to the thermal treatment. Figure 5 shows the obtained curves. It shows a mass loss of 80% in two stages: 35% from the ambient temperature to 200 °C and 45% from 200 to 300 °C. The first mass loss is associated with dehydration (water from the surface), since the precipitate is in the form of a white paste. It can be said that the first large endothermic peak of the DTA encompasses the phenomena of dehydration and also the phase transitions of NH_4NO_3 that have been observed in the XRD profiles at 70 °C. The same results were reported elsewhere [7,25]. The second DTA endothermic wave is associated with ammonium nitrate boiling and decomposition of both Bi and W precursors. The exothermic peak at 330 °C corresponds to the formation (crystallization) of BWO oxide.

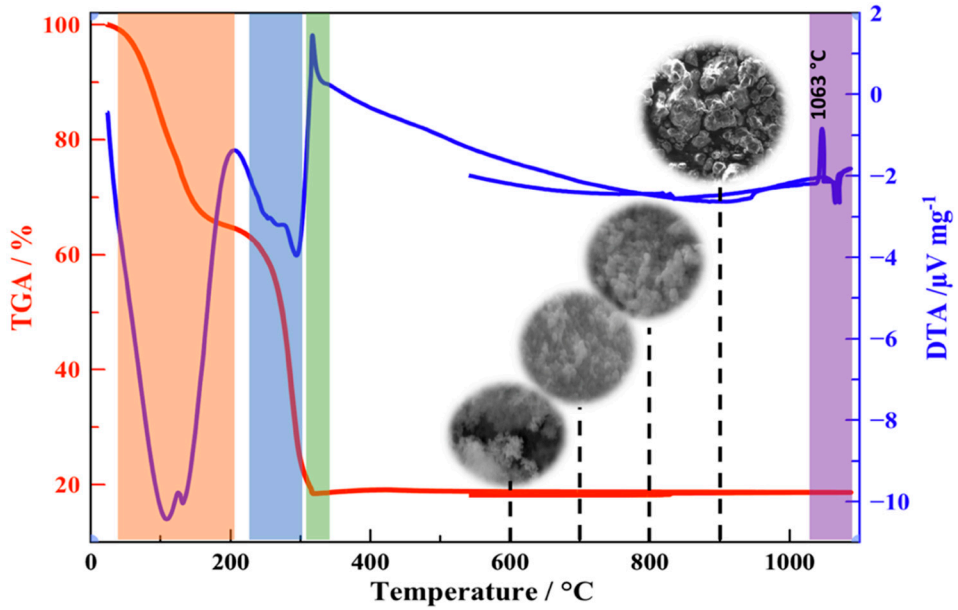

Figure 5. TGA−DTA of the white gel obtained after the coprecipitation method.

2.4. Electrocatalytic Activity

The BWO sample calcined at a low temperature presented the best electrocatalytic activity towards the degradation of the RhB dye. The remaining materials exhibited a temperature-dependent degradation efficiency (Figure 6a). This might be due to crystallite size, surface area, and eventually the morphology of electrocatalysts. Figure 6b illustrates the evolution of the degradation efficiency as a function of the geometrically calculated area of the particles. We observe that the electroactivity of the electrode catalysts has the same trend as the evolution of the geometrically calculated surface area. The trend argues in favor of a synergistic effect between the surface area and the morphology of the samples. This leads us to conclude that the enhanced efficiency of the BWO-600 samples is principally due to their high surface area, morphology, and good adherence to the GC electrode surface. It is worth noting that the bare GCE electrode has only 25% degradation for 30 min of electrolysis.

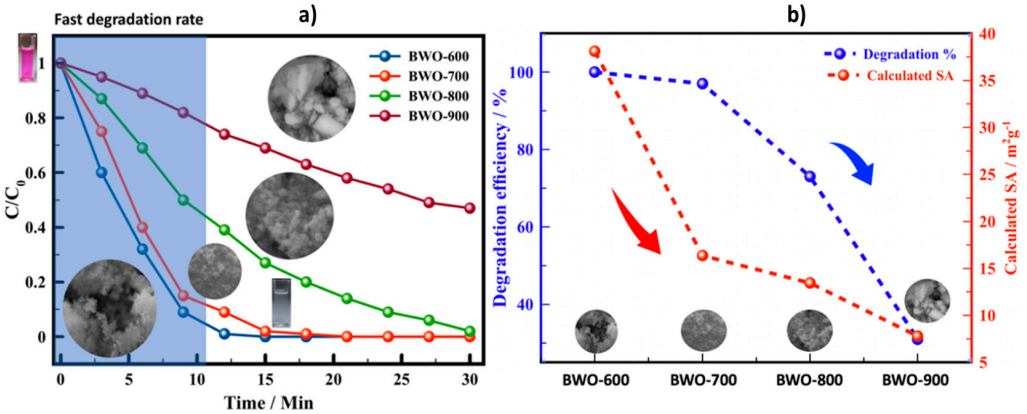

Figure 6. (**a**) Electrocatalytic activity of the prepared BWO samples at different temperatures and (**b**) evolution of degradation efficiency as a function of calculated surface area.

We have further investigated the best working electrode, BWO-600, by changing pollutant concentration, supporting electrolyte, and current density. Figure 6a shows the effect of the current density on the electrodegradation of 10 ppm of RhB dye. It is well known that increasing current density is a key factor to generate the hydroxyl groups, chlorine and hypochlorite species thus promoting electrodegradation (can be applied also

in electrophotocatalysis) [26,27]. This explains the increase in the RhB degradation from 5 to 10 mA/cm^{-2} in which optimal chlorine species and hydroxyl radicals were produced. However, in some cases where the electrode's oxygen evolution potential (OEP) is not higher than the oxygen evolution reaction (OER), the degradation will be inhibited by the overwhelming oxygen/chlorine bubbles evolving from the electrode's surface, making it harder for the organic molecules to reach the surface of the active electrode [28,29]. This leads to a mass transport limiting step and low bulk degradation of the RhB molecule. We have performed a series of BWO/GCE loadings ranging from 10^{-9} to 9 10^{-8} mol cm^{-2} to evaluate the effect of the BWO on the electrocatalytic activity (Figure 7b). We observed that at lower loadings, the Rhb can be degraded with an efficiency of 83%. The dye's degradation was increased by increasing the BWO loading, reaching a maximum of 5 $\times$ 10^{-8} mol cm^{-2}. This shows an optimal loading quantity for efficient RhB electro-oxidation. A further increase of the loading to 9 $\times$ 10^{-8} mol cm^{-2} deteriorated the efficiency due to the observed peeling-off of the BWO from the GCE surface in reaction conditions.

Figure 7c illustrates the electrodegradation rates of RhB dye with different concentrations ranging from 5 to 20 ppm. After 9 min, the average degradation efficiencies are almost 97%, 90%, and 25% for the solutions containing 5, 10, and 20 mg L^{-1} of RhB dye. For both 5 and 10 ppm, the degradation efficiencies reached almost 100% after 15 min of electrolysis. At lower RhB concentrations, the dye was degraded at the solid-liquid interface [30], and the electrochemical oxidation was faster than the diffusion of the dye. Whereas, at higher RhB concentrations, the total organic carbon (TOC) is increased, which blocks the generated hydroxyl radicals •OH, thus lowering the electrocatalytic efficiency. The hydroxyl radicals are the rate-limiting step [30,31].

Figure 8a shows the effect of electrolyte solution on the catalytic degradation of RhB dye. As one can see, the electrocatalytic efficiency is more pronounced at 0.1 M of NaCl, while it decreases as we increase the electrolyte concentration. One possible explanation is that increasing the ionic strength leads to a remarkable solution resistance that inhibits the degradation rates. Another explanation is that the formation of chlorine at the anode (Reaction 1) leads to the formation of hypochlorous acid through hydrolysis (Reaction 2): A series of back-diffusion to the electrode might occur, leading to further oxidizing to chlorates. Chlorine might also lead to the formation of organochloride molecules which inhibit degradation at higher Cl_2 content [32,33].

$$2Cl^- \rightarrow Cl_2 + 2e^- \text{ Reaction 1}$$

$$Cl_2 + H_2O \rightarrow HClO + Cl^- + H^+ \text{ Reaction 2}$$

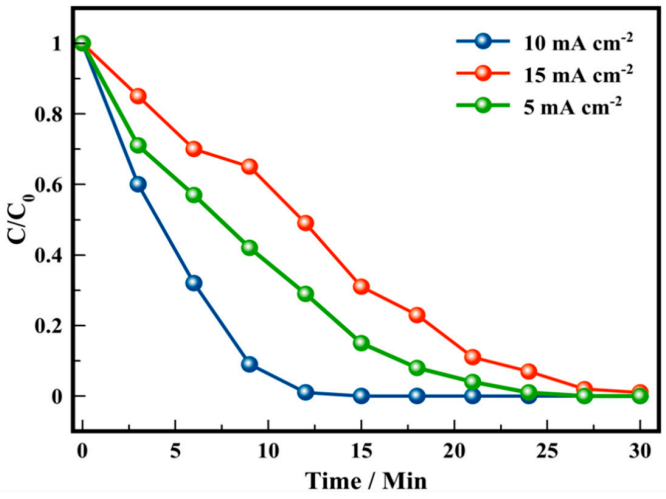

(**a**)

Figure 7. *Cont.*

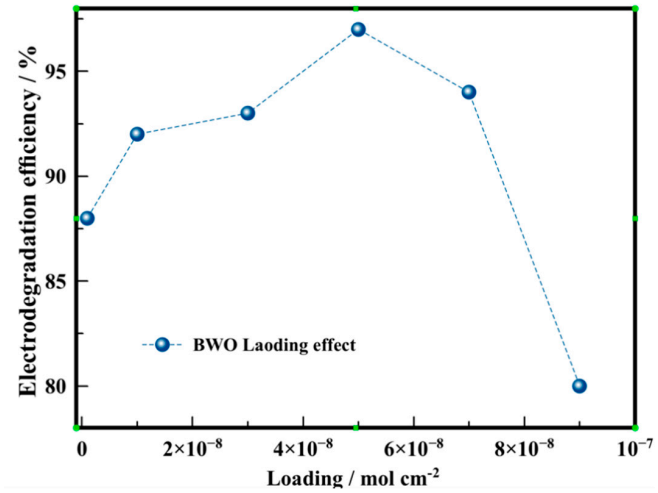

(**b**)

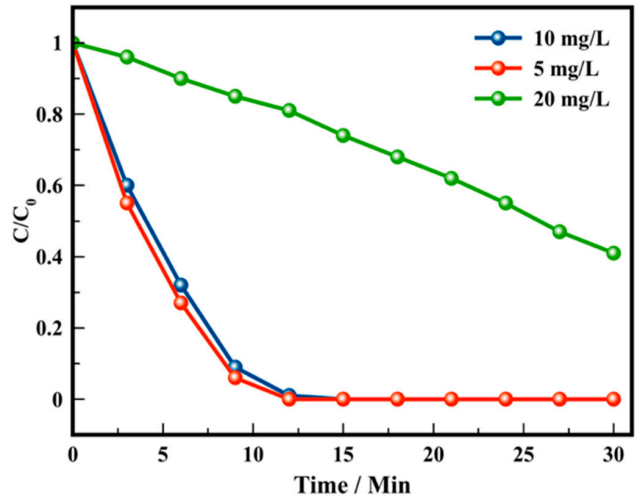

(**c**)

Figure 7. (**a**) The effect of current density on RhB dye degradation efficiency; (**b**) the effect of BWO loading on RhB electrodegradation; and (**c**) the effect of electrolyte concentration on RhB oxidation.

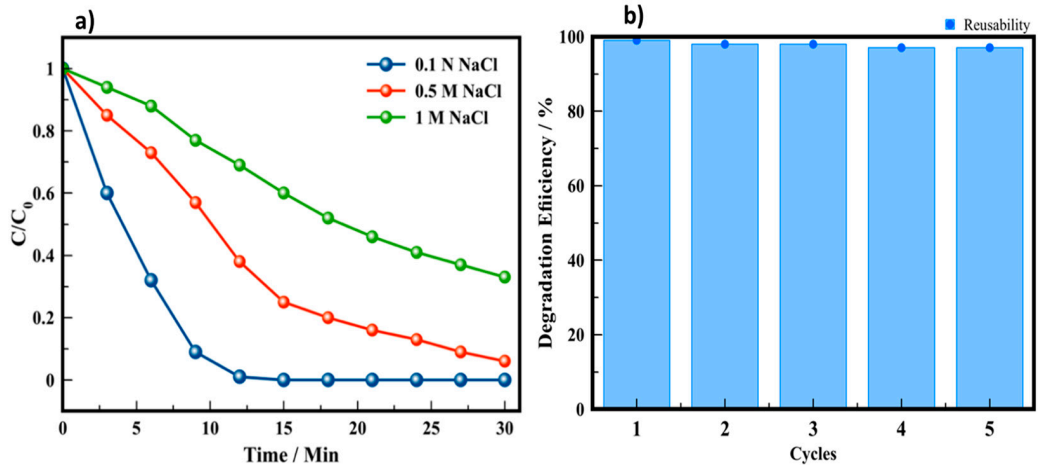

Figure 8. (**a**) Supporting electrolyte effect on electrocatalytic activity and (**b**) reusability cycles of the BWO-600 electrode.

3. Materials Synthesis

This process consists of dissolving a quantity of bismuth nitrate (Aldrich, 99.9%) in distilled water and nitric acid (10% *v/v*). After stirring for 30 min, a transparent, colorless solution is obtained. A progressive addition of 5 mL/min of hydrated ammonium tungstate ($(NH_4)_6W_7O_{24}.6H_2O$) to this solution is carried out dropwise, and by maintaining the agitation, a white solution is formed progressively by the addition of the tungstate solution. Then, the pH of the solution is adjusted by the addition of NH_4OH (d = 0.91) until about 5, and the solution is put in evaporation at 70 °C until obtaining the white paste, which was analyzed by ATD/ATG (also analyzed after drying at 70 °C), then calcined at 600, 700, 800, and 900 °C.

4. Characterization Methods

For X-ray diffraction analysis, the apparatus used is a PANALYTICAL EMPYREAN, equipped with a copper anticathode bombarded by accelerated electrons at a voltage of 45 kV, the current being 35 mA.

Scanning electron microscopy (SEM) analyses were performed using an Hitachi S-4700 SEM. Energy dispersive spectroscopy and elemental mapping were carried out to compare the experimental composition to nominal synthesis concentrations.

Thermogravimetry analysis (TGA) coupled with differential thermal analysis (DTA) was performed on the decomposition of the precursor, which was followed under air between 25 and 1150 °C with a rate of 10 °C/min (using Shimadzu Instruments DTG-60 equipment).

Electrochemical analysis was performed using a VoltaLab PGZ 301 equipped with Volta Master 4 software. A conventional three-electrode thermostatically controlled glass cell filled with 100 cm^3 of solution was used. A BWO thin film working electrode and ECS as a reference electrode were used while the counter electrode is platinum wire. The electrodes were the prepared BWO powders deposited on a glassy carbon electrode (GCE) substrate, while the cathode was a platinum electrode. The films were prepared by dissolving a given amount of BWO powder in methanol and drop-coated on a glassy carbon substrate. The BWO/GCE working electrodes were dried before use. The ICP was used to check the loading of electrocatalysts. An amount of 5 10^{-8} mol cm^{-2} was calculated. A saturated calomel electrode (SCE) was used as a reference electrode, and all the reported potentials are against SCE. The duration of electrocatalysis was 30 min. The UV-visible spectra were recorded using a UV-Vis spectrometer. The samples were taken every 3 min during electrodegradation.

A comparative study of the prepared BWO samples was carried out using the BWO active electrodes to perform electrode degradation of 10 mg/L^{-1} solution of Rhodamine B containing 0.1 mol/ L^{-1} NaCl. This latter was added as a supporting electrolyte. The current density during the degradation was kept constant at 10 mA/cm^{-2}.

5. Conclusions

As a summary, we have successfully synthesized Bi_2WO_6 at different temperatures using a simple co-precipitation method. The powerful Rietveld method was adopted to refine the crystallographic parameters. It was found that the prepared BWO materials crystallize in orthorhombic single-phase structures with the $Pca2_1$ space group. The BWO-600 presented the highest electrocatalytic activity for RhB degradation in near neutral conditions (pH = 7.1). The effects of current density, RhB concentration, and supporting electrolyte were studied. The electrodegradation rates of RhB dye with different concentrations range from 5 to 20 ppm. After 9 min, the average degradation efficiencies are almost 97%, 90%, and 25% for the solutions containing 5, 10, and 20 mg L^{-1} of RhB dye. The best working environments are 0.1 M NaCl, 10 mA cm^{-2} and 5–10 mg L^{-1} of the dye. The BWO-600 showed its reusability up to 4 cycles of reuse under the reported conditions and illustrated an electrocatalytic degradation of more than 90%. This indicates the prominent application of BWO-600 as a versatile and universal electrode for faster water decontamination.

Author Contributions: Writing—original draft, preparation and characterization of materials, editing, supervision, validation, and visualization, H.A.A. and A.B. (Amal BaQais); writing, editing, supervision, validation, and visualization, M.A.; SEM and mapping characterization, editing, and reviewing, B.B. and A.B. (Abdeljalil Benlhachemi). All authors have read and agreed to the published version of the manuscript.

Funding: Princess Nourah bint Abdulrahman University Researchers Supporting Project number (PNURSP2022R230), Princess Nourah bint Abdulrahman University, Riyadh, Saudi Arabia.

Acknowledgments: The authors acknowledge the Princess Nourah bint Abdulrahman University Researchers Supporting Project number PNURSP2022R230, Princess Nourah bint Abdulrahman University, Riyadh, Saudi Arabia.

Conflicts of Interest: The authors declare no conflict of interest.

References

1. Priya, A.M.; Selvan, R.K.; Senthilkumar, B.; Satheeshkumar, M.K.; Sanjeeviraja, C. Synthesis and Characterization of $CdWO_4$ Nanocrystals. *Ceram. Int.* **2011**, *37*, 2485–2488. [CrossRef]
2. Chen, S.-H.; Yin, Z.; Luo, S.-L.; Li, X.-J.; Yang, L.-X.; Deng, F. Photoreactive Mesoporous Carbon/Bi_2WO_6 Composites: Synthesis and Reactivity. *Appl. Surf. Sci.* **2012**, *259*, 7–12. [CrossRef]
3. Knight, K.S. The Crystal Structure of Russellite; a Re-Determination Using Neutron Powder Diffraction of Synthetic Bi_2WO_6. *Mineral. Mag.* **1992**, *56*, 399–409. [CrossRef]
4. Zeng, T.; Yan, H.; Ning, H.; Zeng, J.; Reece, M.J. Piezoelectric and Ferroelectric Properties of Bismuth Tungstate Ceramics Fabricated by Spark Plasma Sintering. *J. Am. Ceram. Soc.* **2009**, *92*, 3108–3110. [CrossRef]
5. Yoneda, Y.; Kohara, S.; Takeda, H.; Tsurumi, T. Local Structure Analysis of Bi_2WO_6. *Jpn. J. Appl. Phys.* **2012**, *51*, 09LE06. [CrossRef]
6. He, Z.; Sun, C.; Yang, S.; Ding, Y.; He, H.; Wang, Z. Photocatalytic Degradation of Rhodamine B by Bi_2WO_6 with Electron Accepting Agent under Microwave Irradiation: Mechanism and Pathway. *J. Hazard. Mater.* **2009**, *162*, 1477–1486. [CrossRef]
7. Alfaro, S.O.; Martínez-de La Cruz, A. Synthesis, Characterization and Visible-Light Photocatalytic Properties of Bi_2WO_6 and $Bi_2W_2O_9$ Obtained by Co-Precipitation Method. *Appl. Catal. A Gen.* **2010**, *383*, 128–133. [CrossRef]
8. Li, Y.; Liu, J.; Huang, X. Synthesis and Visible-Light Photocatalytic Property of Bi_2WO_6 Hierarchical Octahedron-Like Structures. *Nanoscale Res. Lett.* **2008**, *3*, 365–371. [CrossRef]
9. Wang, C.; Zhu, L.; Wei, M.; Chen, P.; Shan, G. Photolytic Reaction Mechanism and Impacts of Coexisting Substances on Photodegradation of Bisphenol A by Bi_2WO_6 in Water. *Water Res.* **2012**, *46*, 845–853. [CrossRef] [PubMed]
10. Amano, F.; Nogami, K.; Ohtani, B. Enhanced Photocatalytic Activity of Bismuth-Tungsten Mixed Oxides for Oxidative Decomposition of Acetaldehyde under Visible Light Irradiation. *Catal. Commun.* **2012**, *20*, 12–16. [CrossRef]
11. Ait Ahsaine, H.; El jaouhari, A.; Slassi, A.; Ezahri, M.; Benlhachemi, A.; Bakiz, B.; Guinneton, F.; Gavarri, J.-R. Electronic Band Structure and Visible-Light Photocatalytic Activity of Bi_2WO_6: Elucidating the Effect of Lutetium Doping. *RSC Adv.* **2016**, *6*, 101105–101114. [CrossRef]
12. Ait Ahsaine, H. UV-Light Photocatalytic Properties of the Bismuth Lutetium Tungstate System $Bi_{2-X}Lu_xWO_6$ ($0 \leq x \leq 1$). *Mater. Lett.* **2020**, *276*, 128221. [CrossRef]
13. Anfar, Z.; Ait Ahsaine, H.; Zbair, M.; Amedlous, A.; Ait El Fakir, A.; Jada, A.; El Alem, N. Recent Trends on Numerical Investigations of Response Surface Methodology for Pollutants Adsorption onto Activated Carbon Materials: A Review. *Crit. Rev. Environ. Sci. Technol.* **2020**, *50*, 1043–1084. [CrossRef]
14. Ait Ahsaine, H.; Ezahri, M.; Benlhachemi, A.; Bakiz, B.; Villain, S.; Guinneton, F.; Gavarri, J.-R. Novel Lu-Doped Bi_2WO_6 Nanosheets: Synthesis, Growth Mechanisms and Enhanced Photocatalytic Activity under UV-Light Irradiation. *Ceram. Int.* **2016**, *42*, 8552–8558. [CrossRef]
15. Anfar, Z.; Zbair, M.; Ait Ahsiane, H.; Jada, A.; El Alem, N. Microwave Assisted Green Synthesis of Fe_2O_3/Biochar for Ultrasonic Removal of Nonsteroidal Anti-Inflammatory Pharmaceuticals. *RSC Adv.* **2020**, *10*, 11371–11380. [CrossRef]
16. Lotfi, S.; El Ouardi, M.; Ahsaine, H.A.; Assani, A. Recent Progress on the Synthesis, Morphology and Photocatalytic Dye Degradation of $BiVO_4$ Photocatalysts: A Review. *Catal. Rev.* **2022**, 1–45. [CrossRef]
17. Altass, H.M.; Morad, M.; Khder, A.E.-R.S.; Mannaa, M.A.; Jassas, R.S.; Alsimaree, A.A.; Ahmed, S.A.; Salama, R.S. Enhanced Catalytic Activity for CO Oxidation by Highly Active Pd Nanoparticles Supported on Reduced Graphene Oxide /Copper Metal Organic Framework. *J. Taiwan Inst. Chem. Eng.* **2021**, *128*, 194–208. [CrossRef]
18. Alshorifi, F.T.; Alswat, A.A.; Salama, R.S. Gold-Selenide Quantum Dots Supported onto Cesium Ferrite Nanocomposites for the Efficient Degradation of Rhodamine B. *Heliyon* **2022**, *8*, e09652. [CrossRef]
19. Ahsaine, H.A.; Slassi, A.; Naciri, Y.; Chennah, A.; Jaramillo-Páez, C.; Anfar, Z.; Zbair, M.; Benlhachemi, A.; Navío, J.A. Photo/Electrocatalytic Properties of Nanocrystalline ZnO and La–Doped ZnO: Combined DFT Fundamental Semiconducting Properties and Experimental Study. *ChemistrySelect* **2018**, *3*, 7778–7791. [CrossRef]
20. Awad, H.S.; Galwa, N.A. Electrochemical Degradation of Acid Blue and Basic Brown Dyes on Pb/PbO_2 Electrode in the Presence of Different Conductive Electrolyte and Effect of Various Operating Factors. *Chemosphere* **2005**, *61*, 1327–1335. [CrossRef]

21. Xu, X.; Wu, C.; Ye, J.; Fan, P. Enhanced Coagulation by Diatomite Blends Based on Zeta Potential. *Environ. Sci. Technol.* **2010**, *33*, 151–165.
22. Zhang, F.-J.; Liu, J.; Chen, M.-L.; Oh, W.-C. Photoelectrocatalytic Degradation of Dyes in Aqueous Solution Using CNT/TiO_2 Electrode. *J. Korean Ceram. Soc.* **2009**, *46*, 263–270. [CrossRef]
23. Bessegato, G.G.; Cardoso, J.C.; Zanoni, M.V.B. Enhanced Photoelectrocatalytic Degradation of an Acid Dye with Boron-Doped TiO_2 Nanotube Anodes. *Catal. Today* **2015**, *240*, 100–106. [CrossRef]
24. Suhadolnik, L.; Pohar, A.; Likozar, B.; Čeh, M. Mechanism and Kinetics of Phenol Photocatalytic, Electrocatalytic and Photoelectrocatalytic Degradation in a TiO_2-Nanotube Fixed-Bed Microreactor. *Chem. Eng. J.* **2016**, *303*, 292–301. [CrossRef]
25. Martinez-de La Cruz, A.; Alfaro, S.O. Synthesis and Characterization of γ-Bi_2MoO_6 Prepared by Co-Precipitation: Photoassisted Degradation of Organic Dyes under Vis-Irradiation. *J. Mol. Catal. A Chem.* **2010**, *320*, 85–91. [CrossRef]
26. Amaterz, E.; Tara, A.; Bouddouch, A.; Taoufyq, A.; Bakiz, B.; Lazar, F.; Gilliot, M.; Benlhachemi, A.; Bazzi, L.; Jbara, O. Hierarchical Flower-like $SrHPO_4$ Electrodes for the Photoelectrochemical Degradation of Rhodamine B. *J. Appl. Electrochem.* **2020**, *50*, 569–581. [CrossRef]
27. Chennah, A.; Naciri, Y.; Ahsaine, H.A.; Taoufyq, A.; Bakiz, B.; Bazzi, L.; Guinneton, F.; Gavarri, J.-R.; Benlhachemi, A. Electrocatalytic Properties of Hydroxyapatite Thin Films Electrodeposited on Stainless Steel Substrates. *Mediterr. J. Chem.* **2018**, *6*, 255–266. [CrossRef]
28. Wu, J.-C.; Chuang, Y.-H.; Liou, S.Y.H.; Li, Q.; Hou, C.-H. In Situ Engineering of Highly Conductive TiO_2/Carbon Heterostructure Fibers for Enhanced Electrocatalytic Degradation of Water Pollutants. *J. Hazard. Mater.* **2022**, *429*, 128328. [CrossRef]
29. Zhang, Y.; He, P.; Jia, L.; Li, C.; Liu, H.; Wang, S.; Zhou, S.; Dong, F. Ti/PbO_2-Sm_2O_3 Composite Based Electrode for Highly Efficient Electrocatalytic Degradation of Alizarin Yellow R. *J. Colloid Interface Sci.* **2019**, *533*, 750–761. [CrossRef]
30. Martínez-Huitle, C.A.; Brillas, E. Decontamination of Wastewaters Containing Synthetic Organic Dyes by Electrochemical Methods: A General Review. *Appl. Catal. B Environ.* **2009**, *87*, 105–145. [CrossRef]
31. Lucas, M.S.; Peres, J.A. Decolorization of the Azo Dye Reactive Black 5 by Fenton and Photo-Fenton Oxidation. *Dye. Pigment.* **2006**, *71*, 236–244. [CrossRef]
32. Souza, F.L.; Aquino, J.M.; Irikura, K.; Miwa, D.W.; Rodrigo, M.A.; Motheo, A.J. Electrochemical Degradation of the Dimethyl Phthalate Ester on a Fluoride-Doped Ti/β-PbO_2 Anode. *Chemosphere* **2014**, *109*, 187–194. [CrossRef] [PubMed]
33. Comninellis, C. Electrocatalysis in the Electrochemical Conversion/Combustion of Organic Pollutants for Waste Water Treatment. *Electrochim. Acta* **1994**, *39*, 1857–1862. [CrossRef]